Research Square

Preprints are preliminary reports that have not undergone peer review.
They should not be considered conclusive, used to inform clinical practice,
or referenced by the media as validated information.

Underwater Explosion Shock Waves Reflected from Sandy Bottoms: Theoretical Modeling and Damage Zone Evolution

Jifeng Wei

weijifeng@bit.edu.cn

Beijing Institute of Technology

Xingwei Liu

Beijing Institute of Technology

Yuxuan Zheng

Beijing Institute of Technology

Fangfei Ren

Beijing Institute of Technology

Junjie Xiao

Beijing Institute of Technology

Jialin Zhu

Beijing Institute of Technology

Research Article

Keywords: Underwater explosion, Sandy seabed reflection, Residual reflection coefficient, Damage zone

Posted Date: November 27th, 2026

DOI: https://doi.org/10.21203/rs.3.rs-11811657/v1

License: This work is licensed under a Creative Commons Attribution 4.0 International License.
Read Full License

Additional Declarations: No competing interests reported.

Underwater Explosion Shock Waves Reflected from Sandy Bottoms: Theoretical Modeling and Damage Zone Evolution

Jifeng Wei [a*], Xingwei Liu [a], Yuxuan Zheng [a], Fangfei Ren [a], Junjie Xiao [a], Jialin Zhu [a]

[a] State Key Laboratory of Explosion Science and Safety Protection, Beijing Institute of Technology, Beijing 100081, China

[*]Corresponding author. E-mail address: weijifeng@bit.edu.cn (Jifeng Wei)

Abstract

Underwater explosion (UNDEX) loads on submerged structures and personnel are usually predicted with the seabed either ignored or treated as a rigid wall, so that the wave returned by the bottom is misplaced in both amplitude and arrival time. A reflection model for a saturated sand half-space combines the image method with the velocity–pressure (*u*–*p*) equations of water and sand. The ratio of the calculated reflection coefficient to its ideal rigid-wall value defines a residual reflection coefficient η, expressed as a function of charge mass, stand-off height and incident angle. Fitted to 44 arbitrary Lagrangian–Eulerian simulations covering 1–150 g, 0.1–0.3 m and 0–60°, it reproduces 16 gauge records from six tank tests with a mean absolute deviation of 8.8%. η stays nearly constant up to about 40°, falls steeply thereafter, and vanishes near the critical angle of 62°, where the transmitted longitudinal wave degenerates into an interface wave. Applied to impulse-based injury criteria, the model gives, for a 5 kg charge at a stand-off of 200 m, a maximum mild-injury radius of 416.5 m instead of 215.5 m in the free field, a factor of 1.93; reflection alone accounts for 1.19 of that factor. At 250 m from the axis the impulse rises from 106.2 to 182.4 kPa·ms, lifting a location that the conventional estimate leaves below the mild-injury threshold into the moderate-injury range.

Keywords: Underwater explosion; Sandy seabed reflection; Residual reflection coefficient; Damage zone

1 Introduction

UNDEX is widely utilized in the marine engineering and defense fields, such as subsea reef clearance, offshore platforms removal and underwater obstacle demolition [1, 2]. During these subsea operations, the extremely high-pressure shock wave and oscillating bubble generated by UNDEX are main damage loads on target structures, inevitably posing severe threats to adjacent marine infrastructure and operational personnel [3, 4]. It is of great significance to study the propagation mechanisms of UNDEX shock waves and the ensuing transient fluid-structure interactions (FSI), which can provide important guidance whether for blast load prediction and structural integrity analysis or for safety assessment.

Extensive theoretical and experimental studies have shown a relatively clear recognition for UNDEX phenomena. The propagation of shock waves in free-field conditions and their interactions with

boundaries have attracted great concern. Cole [5] made a systematic conclusion of underwater explosion in 1948, which revealed that the peak pressure of shock wave is primarily influenced by charge weight and standoff. Zamyshlyaev [6] had proposed a theoretical correction to study the reflection characteristics of shock waves with free liquid surface and ideal rigid water bottom. With the advancements in computational mechanics and equations of state (EOS), Arbitrary Lagrangian-Eulerian (ALE) algorithm has been widely adopted to explore the transient FSI responses or cumulative structural damages of targets subjected to near-field or multiple sequential detonations [7, 8]. Furthermore, highly nonlinear bubble dynamics, jetting phenomena, and multiphase flow characteristics within compressible fluids have been studied extensively [9, 10]. However, the theoretical frames are mainly based on the assumptions of homogeneous single medium and ideal rigid boundary [11], which inherently can represent neither the energy dissipation behavior in the process of shock wave propagation nor acoustic impedance of real seabed.

Considering that the seabed is a kind of saturated porous medium, researchers have started to investigate the effects of strong fluid-solid coupling influenced by non-rigid, compressible seabed [12, 13]. Yan et al. [14] derived a Hugoniot expression related to the transmission and reflection of shock wave at the water-soil interface, from which the exact analytical solutions can be obtained. Recent numerical simulations and machine learning investigations have demonstrated that the reflection wave and bubble behavior can be deeply influenced by the characteristics of seabed [15, 16]. Nevertheless, the study on reflection wave with non-rigid bottom is still scarce. For now, the UNDEX safety evaluation is still inaccurate with the distortion of overpressure prediction under complex boundary condition.

In this study, a theoretical analysis model of shock wave propagation is proposed with the consideration of shock wave seabed reflection. The UNDEX experiments and ALE fluid-solid coupling numerical simulations are carried out to explore the spatial distributions of shock waves by reflected seabed, thus a multi-parameter, nonlinear empirical formula for the residual reflection coefficient (η) is yielded. Moreover, this new formula is applied to quantitatively evaluate the spatial evolution of blast-induced injury zones in reflective environments. These results can reveal the underlying physical mechanisms of reflection wave superposition in complex underwater environments, which provides a robust, quantitative theoretical method for high-precision blast load prediction and personnel safety assessment in practical marine operations.

2 Theoretical model of UNDEX shock wave with reflection superposition

2.1 Pressure time-history superposition model based on image method

To obtain the pressure variation process at a point in water, the following assumptions are made:

(1) The explosive charge is regarded as a mass point;

(2) The regular reflection is considered in the propagation process of shock wave and Mach reflection is ignored;

(3) The shock wave front remains spherical after that the charge is detonated;

(4) The initiation position is far from the water surface, so the influence of free surface reflection effect can be ignored.

The shock wave at any point in water is actually a superimposed wave formed by direct wave and reflection wave from the water bottom. According to the independence of wave, the two parts of superimposed wave are analyzed separately below.

2.1.1 Computational method of direct wave pressure

The horizontal direction along water bottom plane is defined as the x-axis, and the vertical direction passing through the explosive charge is defined as the y-axis, as shown in Fig. 1. The coordinate of explosive charge center O_1 is (0, H) and that of the target point P is (d, h).

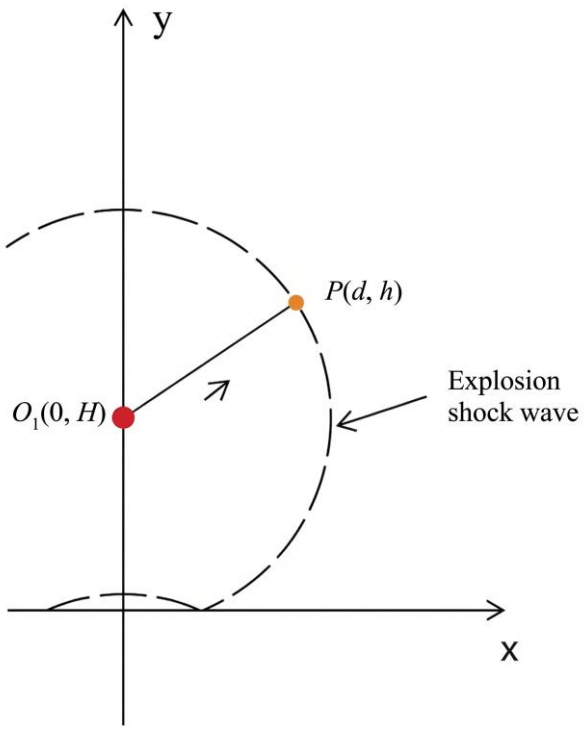

Fig. 1 Schematic diagram of explosion shock wave propagation

The time when direct wave reaches target point P is set to t=0. The computational formula for

UNDEX shock wave pressure $P_{p1}(t)$ [17]at the target point P can be described as,

$$P_{p1}(t) = \begin{cases} P_{m1}(t)e^{-\frac{t}{\theta}} & 0 \le t \le \theta \\ 0.368P_{m1}\frac{\theta}{t} & \theta \le t \le 10\theta \end{cases}, \quad (1)$$

$$P_{m1} = \begin{cases} 44.1(\frac{r}{W^{1/3}})^{-1.5} & 6 \le \frac{r}{r_1} \le 12 \\ 52.4(\frac{r}{W^{1/3}})^{-1.13} & 12 \le \frac{r}{r_1} \le 240 \end{cases}, \quad (2)$$

$$\theta = B(\frac{r}{r_1})^{\alpha_1}\frac{r_1}{c}, \quad (3)$$

$$r = \sqrt{d^2 + (H-h)^2}, \quad (4)$$

where P_{m1} is the peak pressure of direct shock wave (MPa); W is charge equivalent (kg); θ is attenuation constant (s); r represents the distance from explosion center to target point (m); r_1 is the initial radius of explosive charge (m); c is the speed of sound in water (m/s); B and α_1 are constants given by experiments; H is the vertical distance from O_1 to the x-axis (m); d is the horizontal distance from P to the y-axis (m); h is the vertical distance from P to the x-axis (m).

2.1.2 Computational method of reflection wave pressure

The reflection wave at P is the shock wave travelling from O_1 to the bottom (x-axis) and then reflecting back to point P. The trajectory of reflection wave can be acquired with image method. Here, the rigid reflection wall is assumed as a symmetry surface and then a virtual explosion center is established on the other side of the reflection surface. Assuming the reflection wave front is an arc centered on point $O_2(0, -H)$, the intersection point of O_2P and the x-axis is denoted as P_r. Thus, the propagation path can be divided into three parts: from O_1 to P_r (O_1P_r), reflection at point P_r, from P_r to P (P_rP), which are shown in Fig. 2.

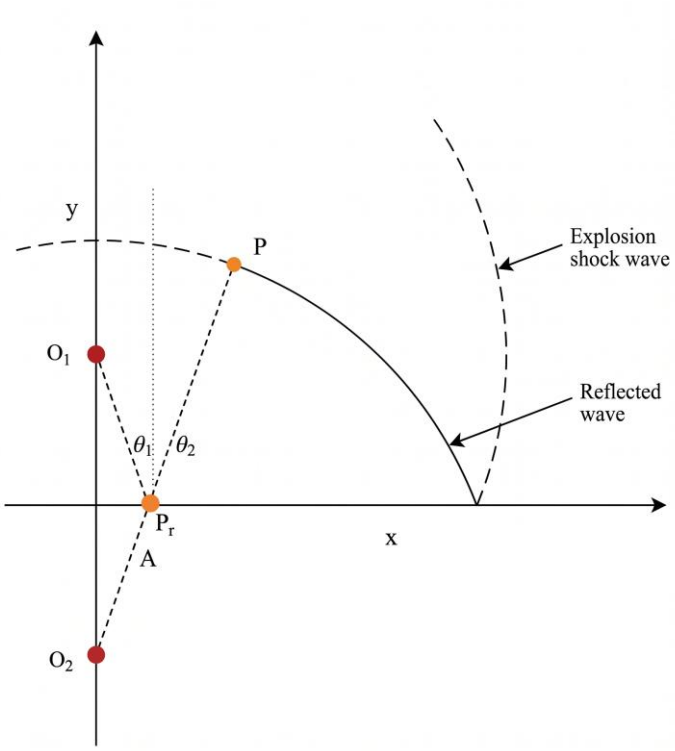

Fig. 2 Schematic diagram of reflection wave propagation

According to Eq. (1) and Eq. (2), the peak pressure of initial explosion shock wave P_{mpr1} and that of virtual explosion shock wave P_{mpr2} at point $\mathrm{P_r}$ can be given as:

$$P_{\mathrm{mpr1}} = \begin{cases} 44.1\left(\frac{r_{\mathrm{O_1P_r}}}{W^{1/3}}\right)^{-1.5} & 6 \le \frac{r_{\mathrm{O_1P_r}}}{r_1} \le 12 \\ 52.4\left(\frac{r_{\mathrm{O_1P_r}}}{W^{1/3}}\right)^{-1.13} & 12 \le \frac{r_{\mathrm{O_1P_r}}}{r_1} \le 240 \end{cases}, \tag{5}$$

and

$$P_{\mathrm{mpr2}} = \begin{cases} 44.1\left(\frac{r_{\mathrm{O_2P_r}}}{W_{\mathrm{r}}^{1/3}}\right)^{-1.5} & 6 \le \frac{r_{\mathrm{O_2P_r}}}{r_2} \le 12 \\ 52.4\left(\frac{r_{\mathrm{O_2P_r}}}{W_{\mathrm{r}}^{1/3}}\right)^{-1.13} & 12 \le \frac{r_{\mathrm{O_2P_r}}}{r_2} \le 240 \end{cases}, \tag{6}$$

where W_{r} is the equivalent of virtual explosive (kg); $r_{\mathrm{O_1P_r}}$ is the distance from $\mathrm{O_1}$ to $\mathrm{P_r}$ (m); $r_{\mathrm{O_2P_r}}$ is the distance from $\mathrm{O_2}$ to $\mathrm{P_r}$ (m); r_2 is the initial radius of the virtual explosive (m).

Here, a new parameter k_{r} is introduced as the reflection coefficient of the shock wave. According to image method, the relationship between P_{mpr2} and P_{mpr1} can be described as:

$$P_{\mathrm{mpr2}} = k_{\mathrm{r}} P_{\mathrm{mpr1}}. \tag{7}$$

Based on symmetrical principle, there is such an expression:

$$r_{\mathrm{O_1P_r}} = r_{\mathrm{O_2P_r}}. \tag{8}$$

Furthermore, the equivalent of virtual explosive charge and the initial radius can be given by Eq. (9) and Eq. (10):

$$W_{\mathrm{r}} = \begin{cases} k_{\mathrm{r}}^2 W & 6 \le \frac{r_{\mathrm{O_2P_r}}}{r_2} \le 12 \\ k_{\mathrm{r}}^{2.66} W & 12 \le \frac{r_{\mathrm{O_2P_r}}}{r_2} \le 240 \end{cases}, \tag{9}$$

$$r_2 = (\frac{3W_r}{4\pi\rho_{TNT}})^{\frac{1}{3}}. \quad (10)$$

So, the peak pressure at point P can be calculated by:

$$P_{m2} = \begin{cases} 44.1(\frac{r_r}{W_r^{\frac{1}{3}}})^{-1.5} & 6 \le \frac{r_r}{r_2} \le 12 \\ 52.4(\frac{r_r}{W_r^{\frac{1}{3}}})^{-1.13} & 12 \le \frac{r_r}{r_2} \le 240 \end{cases}, \quad (11)$$

$$r_r = \sqrt{d^2 + (H+h)^2}, \quad (12)$$

where r_r is the distance from the target point P to the virtual explosive center (m).

The time that the reflection wave reaches target point P is t_r:

$$t_r = \frac{r_r - r}{c}. \quad (13)$$

Therefore, the calculation formula for the reflection wave pressure at point P can be written as:

$$P_{p2}(t) = \begin{cases} P_{m2} e^{-\frac{t-t_r}{\theta_r}} & t_r \le t \le \theta_r + t_r \\ 0.368 P_{m2} \frac{\theta_r}{t-t_r} & \theta_r + t_r \le t \le 10\theta_r + t_r \end{cases}, \quad (14)$$

$$\theta_r = B(\frac{r_r}{r_2})^{\alpha_1} \frac{r_2}{c}, \quad (15)$$

where θ_r is the attenuation constant (s).

In terms of above equations, the total pressure of shock wave at point P can be expressed as:

$$P(t) = \begin{cases} P_{p1}(t), & 0 \le t < t_r \\ P_{p1}(t) + P_{p2}(t), & t \ge t_r \end{cases}. \quad (16)$$

2.2 Computational method of residual reflection coefficient due to sand bottom

The pressure and particle velocity of medium can be expressed using the velocity - pressure (*u-p*) equations. The medium of offshore seabed is mainly composed of saturated sand, whose *u-p* equation [13] can be expressed as:

$$u = \frac{c_s}{4}\left(\sqrt{1 + \frac{8p}{\rho_s c_s^2}} - 1\right), \quad (17)$$

where ρ_s denotes the density of sand (kg/m^3); c_s represents the speed of sound in the sand when the pressure is zero (m/s), with ρ_s = 2210 kg/m^3 and c_s = 1700 m/s for the saturated sand used here.

According to previous study [18], the *u-p* equation of water is given as:

$$u = \frac{c_0}{3.84}\left(\sqrt{1 + \frac{7.68p}{\rho_w c_0^2}} - 1\right), \quad (18)$$

where ρ_w is the density of water (kg/m^3), and c_0 is the speed of sound in water at zero pressure (m/s).

By using the *u-p* equations of water and sand, a group of *u-p* curves can be drawn, as shown in Fig. 3. When the shock wave reaches the interface between water and sand, the incident pressure p_t can be calculated with Eq. (1). Then a symmetric line can be drawn with respect to the particle velocity at this incident pressure, which is just the reflected *u-p* curve of water. At the intersection point of reflected *u-p*

curve of water and the *u-p* curve of sand, the pressure corresponds to the ideal reflection pressure p_{r0}. The ideal reflection pressure neglects transmission losses considering transmission losses during shock reflection.

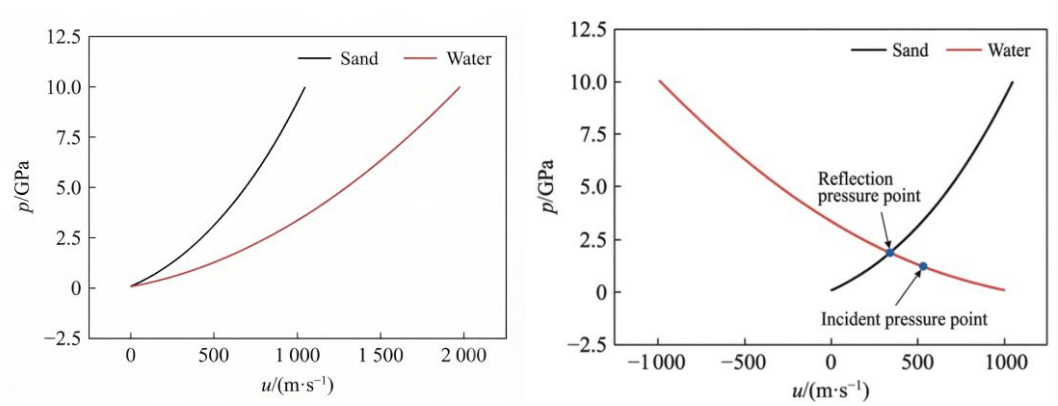

(a) *u-p* Curves of sand and water (b) Ideal reflection pressure at intersection point

Fig. 3 The different curves at reflection interface

The reflection *u-p* curve of water can be expressed as:

$$u = \frac{2c_0}{3.84}\left(\sqrt{1+\frac{7.68p_t}{\rho_w c_0^2}}-1\right)-\frac{c_0}{3.84}\left(\sqrt{1+\frac{7.68p}{\rho_w c_0^2}}-1\right). \tag{19}$$

Combining Eq. (18) and Eq. (19), we obtain:

$$\frac{2c_0}{3.84}\left(\sqrt{1+\frac{7.68p_t}{\rho_w c_0^2}}-1\right)-\frac{c_0}{3.84}\left(\sqrt{1+\frac{7.68p_r}{\rho_w c_0^2}}-1\right)=\frac{c_s}{4}\left(\sqrt{1+\frac{8p_r}{\rho_s c_s^2}}-1\right). \tag{20}$$

The reflection pressure p_r can be solved by Eq. (20), and then the ideal reflection coefficient of sand bottom can be defined as:

$$k_{r0}=\frac{p_r}{p_t}. \tag{21}$$

Due to the energy loss presenting in the interface of real water bottom, the actual reflection coefficient is lower than the ideal one and can be expressed by factoring the ideal one:

$$k_r=\eta k_{r0}=\eta\frac{p_r}{p_t}, \tag{22}$$

where η is the residual reflection coefficient, which can be obtained through experiments or numerical simulation.

3 Experimental and simulation studies on residual reflection coefficient

3.1 Experimental design

In order to study the effects of non-rigid water bottom on shock wave reflection, an UNDEX experimental system is established to obtain real time-history data of reflection waves. It is conducted in a water tank of dimension 1 m×1 m×1.2 m. The water bottom was a layer of ISO 679 standard sand (graded 0.08–2.0 mm) approximately 0.2 m thick. To minimize the reflection interference from the tank

side walls and bottom, a kind of closed-cell polyethylene foam is attached to these inner surfaces. The charges were pressed TNT cylinders with a length-to-diameter ratio of 1:1. The two charge masses used, 1.2×10^{-3} kg and 4.2×10^{-3} kg, correspond to diameters of 9.8 mm and 14.9 mm. Each charge was suspended on the central axis of the tank with its center at the prescribed height H above the sand surface, and was detonated at the center of its upper end face. The experimental layout is shown in Fig. 4.

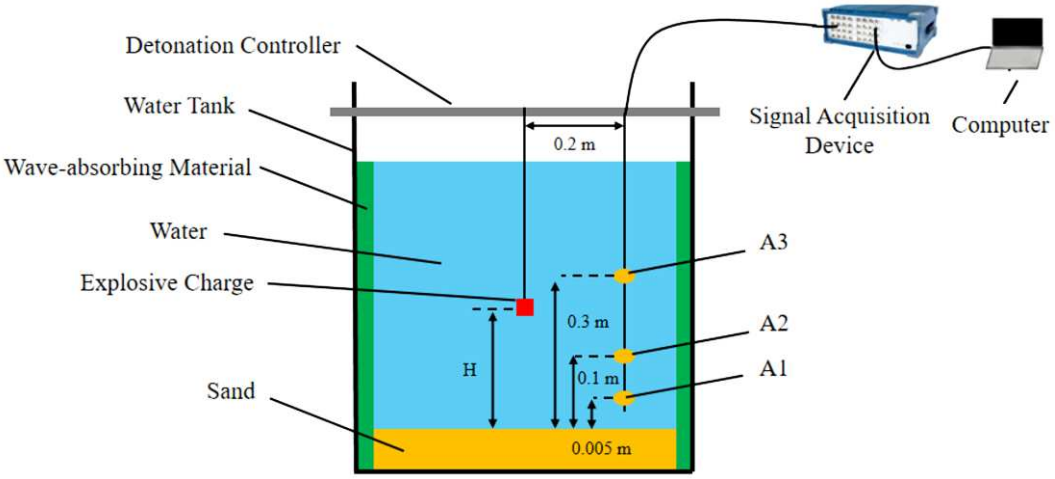

Fig. 4 Schematic diagram of the experimental layout

The pressure acquisition system is composed of sensors, signal acquisition device and computer. An array of underwater sensors is deployed below the water surface, which is connected to the signal acquisition device via the cable of each sensor. Three sensors are named as A1, A2, and A3, which are placed at corresponding locations, as shown in Fig. 4. The acquisition device and the computer are connected with low noise cables. The collected data will be stored in the computer, and the pressure curves will be shown in its screen. Table 1 shows experimental conditions of two explosive charges with different mass.

Table 1 Experimental conditions

Group No.	Explosive mass (kg)	Distance from explosive to bottom (m)	Distance from sensor to bottom (m)
S-1	0.0012	0.2	0.005 (A1) 0.1 (A2) 0.3 (A3)
S-2		0.15	
S-3		0.1	
S-4	0.0042	0.2	
S-5		0.15	
S-6		0.1	

3.2 Experimental results

Six groups of experiments are all implemented as designed, and then corresponding results are all obtained. Taking group S-2 as an example, the pressure curves are explained as follows. The gauge point A1 is very close to the bottom, so the reflection wave can be rapidly superimposed with the direct wave to present a pattern with unimodal distribution. The gauge point A2 is a little far from the bottom, so the reflection wave reaches A2 later than the direct wave, presenting a bimodal pattern. The gauge point A3 is far from the bottom, so the time between two peaks is much longer.

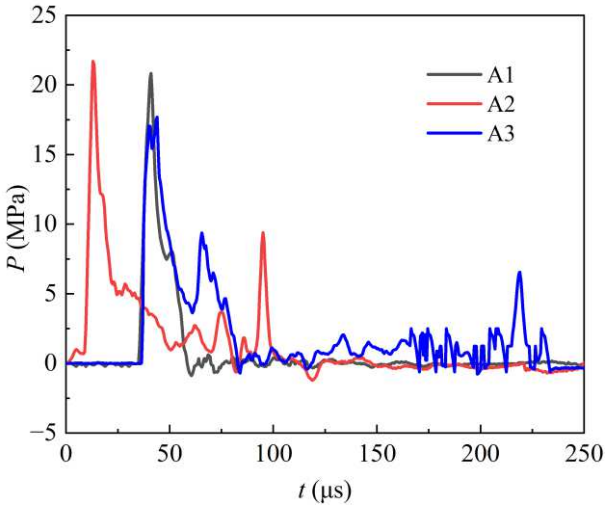

Fig. 5 Pressure-time curve measured in the group S-2

Combining with three curves, the differences among them can be seen very clearly. The wave pattern is decided by the position from explosive center to gauge point characterized by incident angle and propagation path.

Substituting the parameters of explosive center and gauge point and tested results into Eq. (16), the reflection coefficient k_r can be calculated. And then, the ideal reflection coefficient k_{r0} can be gotten with Eq. (21) for each condition. So, the residual reflection coefficient η can be obtained by Eq. (22), which are shown in Table 2.

Table 2 Residual reflection coefficient from experimental results

Group No.	Gauge point	Tested reflection coefficient k_r	Ideal reflection coefficient k_{r0}	Residual reflection coefficient η
S-1	A1	0.480	1.318	0.364
	A2	0.561	1.319	0.425
	A3	0.527	1.319	0.400
S-2	A1	0.206	1.318	0.156
	A2	0.534	1.320	0.405

	A3	0.631	1.321	0.478
	A1	0.049	1.319	0.037
S-3	A2	0.462	1.322	0.349
	A3	0.569	1.324	0.430
	A1	0.311	1.320	0.236
S-4	A2	0.860	1.321	0.651
	A3	0.580	1.322	0.439
	A1	0.156	1.321	0.118
S-5	A2	0.669	1.323	0.506
	A3	0.520	1.324	0.393
	A1	0.022	1.322	0.017
S-6	A2	0.592	1.325	0.447
	A3	0.503	1.328	0.379

Since the velocity of longitudinal wave in sand is higher than that of in water, there exists a critical angle i_c for longitudinal wave when longitudinal wave propagates to the bottom of saturated sand. According to Snell's law [19], there is:

$$i_c = \arcsin\frac{c_0}{c_s} \approx 62°. \tag{23}$$

When the incident angle is less than i_c, the incident wave will be transformed at the interface into reflected longitudinal waves in water, transmitted longitudinal waves in sand and transmitted transverse waves in sand. The clear signal of reflected longitudinal wave can be captured at gauge point in water. Once the incident angle exceeds i_c, the transmitted longitudinal wave will disappear and then turn into a non-uniform wave propagating along the interface. The energy of this non-uniform wave is tightly confined within a thin layer near the interface and cannot be radiated deeply into the sand body, thereby exciting the inherent Scholte wave at the water-sand interface through shear coupling effect [20]. A large amount of incident energy is thus converted into interfacial wave propagating laterally along the interface, which causes a sharp decrease of reflected longitudinal wave energy returned to the water body. According to designed groups, the incident angles of A1 sensors in group S-3 and S-6 are both 62.3°, which exceed the critical longitudinal wave angle and meet the excitation condition of Scholte wave. Therefore, the residual reflection coefficients for those two-gauge points are extremely small.

3.3 Numerical simulation results

3.3.1 Finite element model description

The simulations were performed with LS-DYNA using its ALE2D formulation. The model consists of three materials: water, explosive and sand. Because the tank and the charge are axisymmetric about the vertical axis through the charge, the computational domain is the half-plane section of the tank, 0.5 m wide and 1.2 m high, with the charge axis as the symmetry axis. The domain is discretized with uniform 2 mm elements. The explosive charge is placed at the origin of the coordinate system and the model is symmetric about y-axis. The explosive is modelled as a cylinder with the same dimensions as in the experiment. In the axisymmetric formulation the axial section of the cylinder reduces to a rectangle, which is filled in the ALE mesh by the INITIAL_VOLUME_FRACTION_GEOMETRY keyword. The detonation point is set to the center of charge by the keyword of INITIAL_DETONATION. The keyword of DATABASE_TRACER is adopted to record the shock wave load at gauge points. The finite element model is shown in Fig. 6.

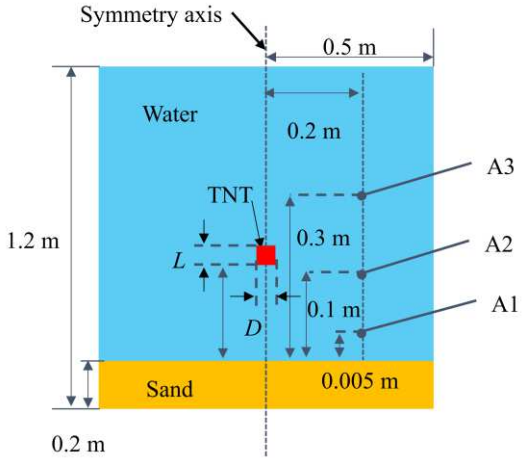

Fig. 6 Axisymmetric finite-element model of the numerical tank. The computational domain is 0.5 m wide and 1.2 m high, with the charge axis as the symmetry axis. The TNT charge is a cylinder of length-to-diameter ratio 1:1, 9.8×10^{-3} m in both diameter D and length L for the 1.2×10^{-3} kg charge, and the charge center is $H = 0.15$ m above the sand surface. A1, A2 and A3 denote the gauge points 0.005, 0.1 and 0.3 m above the sand, on a vertical line 0.2 m from the charge axis. For the 4.2×10^{-3} kg charge, $D = L = 1.49\times10^{-2}$ m.

3.3.2 Material model and equation of state

It is crucial for numerical simulation of UNDEX to select proper equation of state (EOS). The MAT_HIGH_EXPLOSIVE_BURN material model and JWL EOS are utilized for explosive charge, MAT_NULL material model and EOS_LINEAR_POLYNOMIAL equation of state are used for water and MAT_SOIL_AND_FOAM is used for sand.

JWL EOS is often used in hydrocodes to describe the pressure-volume-energy behavior of a detonating explosive, and the pressure is expressed as:

$$p = A\left(1 - \frac{\omega}{R_1 V}\right)\mathrm{e}^{-R_1 V} + B\left(1 - \frac{\omega}{R_2 V}\right)\mathrm{e}^{-R_2 V} + \frac{\omega E_0}{V}, \quad (24)$$

where p is pressure (MPa); V is the relative volume; E is the internal energy of explosive per unit mass; A, B, R_1, R_2 and ω are constants related to the explosive. The parameters of TNT [21] are shown in Table 3.

Table 3 Material parameters of TNT

ρ (g/cm^3)	A (MPa)	B (MPa)	R_1	R_2	ω	E_0 (MPa)	V_0
1.6	3. 738×10^5	3.747×10^3	4.15	0.9	0.35	6.9×10^3	1.0

EOS_LINEAR_POLYNOMIAL of water is given by:

$$p = C_0 + C_1\mu + C_2\mu^2 + C_3\mu^3 + (C_4 + C_5\mu + C_6\mu^2)E, \quad (25)$$

where p is pressure (MPa); $\mu = \rho/\rho_0 - 1$ is the compression ratio defined by the current density ρ and initial density ρ_0; C_0~ C_6 are polynomial equation coefficients; E is internal energy per unit reference volume V_0. The parameters of water [22] are shown in Table 4.

Table 4 Material parameters of water

ρ (g/cm^3)	C_0	C_1	C_2	C_3	C_4	C_5	C_6
1.0	0	0.2002	0.08436	0.0801	0.4394	1.3937	0

MAT_SOIL_AND_FOAM requires input of density, elastic modulus, shear modulus, yield function coefficient, and the stress-volume strain curve of the material, whose suitability for explosion simulation has been verified [23]. The material parameters of sand [23] are shown in Table 5.

Table 5 Material parameters of sand

ρ (g/cm^3)	G (MPa)	K (MPa)	A_0 (MPa^2)	A_1 (MPa)	A_2	p_c (MPa)
2.21	2693	9659	3.339×10^{-7}	0.2251	3.794	-6.9×10^{-3}

3.3.3 Grid-convergence study

Grid convergence was assessed before comparison with the experiments. Four uniformly refined ALE meshes with nominal element sizes of 8, 4, 2, and 1 mm were generated for case S-2. The material models, equations of state, loading, boundary conditions, and output locations were identical in the four calculations. Peak pressures at A1-A3 are plotted in Fig. 7.

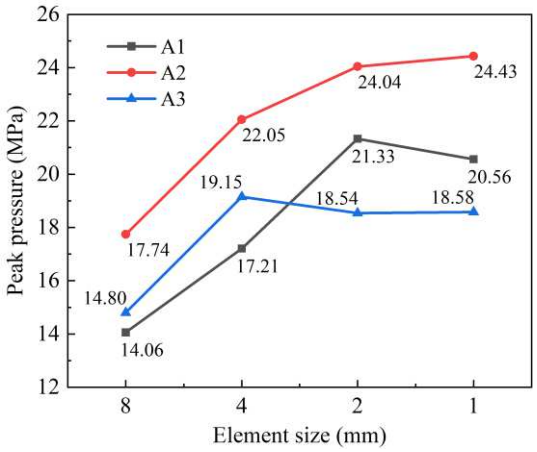

Fig. 7 Grid-convergence curves of peak pressure at gauges A1-A3 for case S-2

The 8-mm mesh underpredicted the peak pressure at all three gauges. The results changed progressively as the mesh was refined, while only small changes occurred between the 2- and 1-mm meshes. Taking the 1-mm solution as the reference, the absolute relative differences obtained with the 2-mm mesh were 3.75%, 1.60%, and 0.22% at A1, A2, and A3, respectively. The A1 and A3 sequences show small non-monotonic variations at the finest resolutions, so the assessment is based on the direct difference between the two finest meshes rather than an assumed monotonic convergence rate.

Because the maximum difference between the 2- and 1-mm solutions was 3.75%, the 2-mm mesh was adopted for the remaining simulations. It provides adequate resolution of the peak pressure while reducing the element count from approximately 6.0×10^5 to 1.5×10^5.

3.3.4 Verification of simulation model

A series of simulations is carried out to get shock wave peak pressures at gauge points. The results of experiments and simulations are all shown in Table 6.

Table 6 The peak pressures of experiments and simulations

Group No.	Gauge point	Experiment		Simulation	
		First peak (MPa)	Second peak (MPa)	First peak (MPa)	Second peak (MPa)
S-1	A1	21.94	/	20.05	/
	A2	20.60	8.52	21.24	8.73
	A3	21.12	5.17	21.77	5.41
S-2	A1	20.84	/	21.33	/
	A2	21.69	9.40	24.04	9.55
	A3	17.48	6.55	18.54	5.92
S-3	A1	21.84	/	20.78	/
	A2	24.08	9.69	25.32	9.98
	A3	16.26	6.75	15.71	6.25

Group No.	Gauge point	Experiment		Simulation	
		First peak (MPa)	Second peak (MPa)	First peak (MPa)	Second peak (MPa)
S-4	A1	32.86	/	34.58	/
	A2	35.27	14.55	36.58	15.17
	A3	40.20	8.90	37.24	9.10
S-5	A1	33.34	/	39.09	/
	A2	39.30	17.84	41.04	16.95
	A3	33.20	9.07	31.83	9.88
S-6	A1	32.89	/	33.04	/
	A2	40.72	18.73	42.73	18.61
	A3	25.52	9.86	26.73	10.08

It can be seen from Fig. 8 that the overpressure waveforms of simulations are in good agreement with those of experiments, which verifies the validity of simulation models.

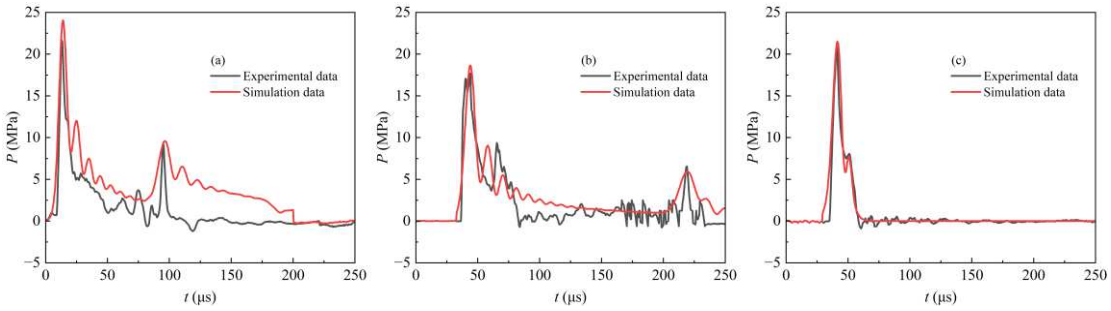

(a) gauge point A1 (b) gauge point A2 (c)gauge point A3

Fig. 8 Comparison of shock wave waveforms for group S-2

According to the data from Table 6, a diagonal scatter diagram of deviation is drawn in Fig. 9. The deviation of all simulation results the deviations are within 20%, with a mean absolute deviation of 8.8%, which demonstrates the accuracy of simulation models.

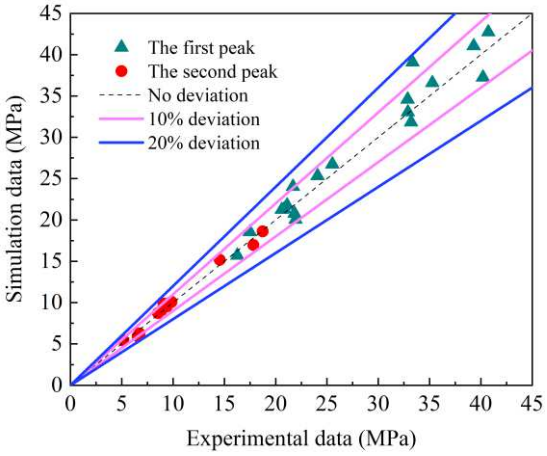

Fig. 9 Diagonal scatter diagram of deviation for experimental and simulated peak pressures

3.4 Simulation results of residual reflection coefficients

According to above analyses, charge equivalent, the distance from charge to bottom, incident angle of shock wave at reflection position are three main factors influencing residual reflection coefficient. A total of 44 simulation studies were conducted, with charge equivalents ranging from 1 g to 150 g, the distance from charge to bottom ranging from 0.1 m to 0.3 m and incident angle ranging from 0° to 60°. The shock wave pressure-time curves for different conditions are obtained, each condition containing 13 curves and each curve involving 13 incident angles. The measured pressure-time curves of shock wave are shown in Fig. 10.

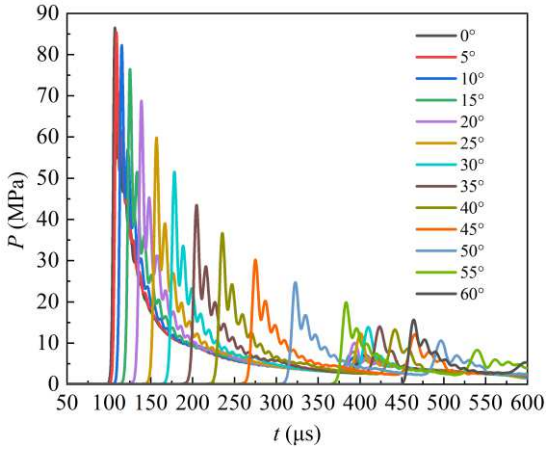

Fig. 10 Pressure-time curves of shock wave

It can be seen that the direct shock wave and the reflected shock wave reach gauge points at different incident angles in sequence, and the peak values of shock wave decrease gradually. Reflection coefficient k_r can be deduced when corresponding parameters are substituted into Eq. (16), while ideal reflection coefficient k_{r0} is derived when parameters are substituted into Eq. (21). So, the residual reflection coefficient η can be obtained, as shown in Fig. 11. The results indicate that residual reflection coefficient fluctuates slightly within the range of incident angle 0 to 40°; the coefficient decreases rapidly when incident angle exceeds 40°, and it approaches 0 for incident angle of 60°.

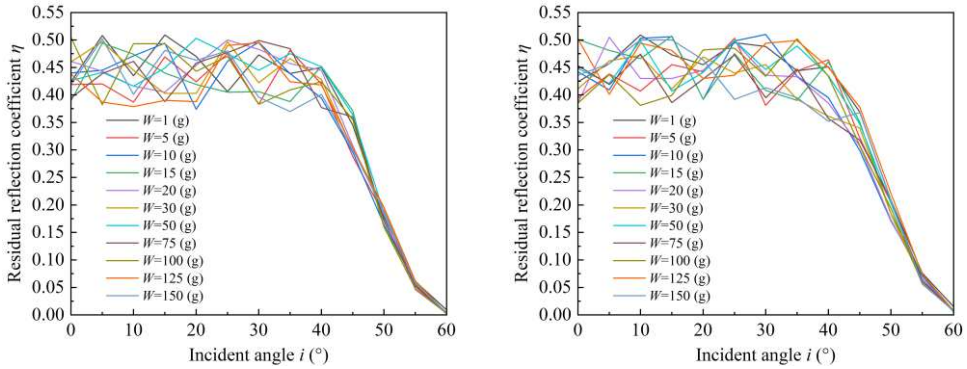

(a) H = 0.10 m (b) H = 0.15 m

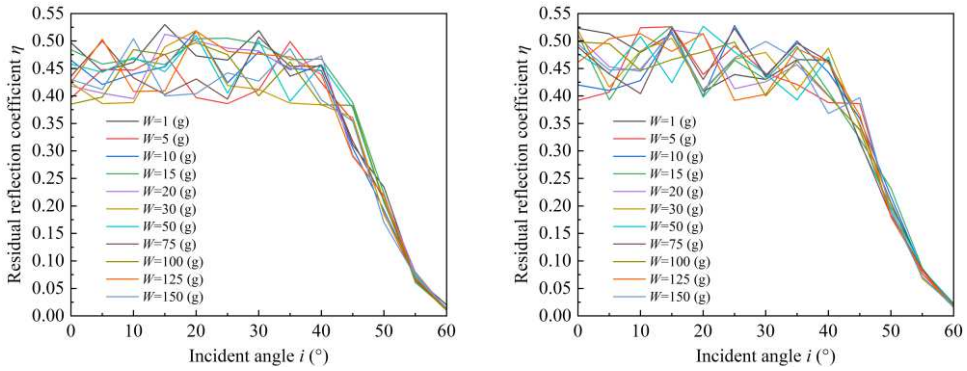

(c) H = 0.2 m (d) H = 0.3 m

Fig. 11 Parameterized evolution of the reflection residual coefficient with incident angle

The residual reflection coefficient is a function of charge equivalent W, the distance from charge to bottom H, incident angle i, so the function expression η (i, W, H) can be determined. With above data, a fitting equation (26) is obtained.

$$\eta(i,W,H)=\left(\frac{0.0184}{1+0.069773\frac{W^{1/3}\cos i}{H}}+\frac{0.2224}{1+0.014190\frac{W^{1/3}\cos i}{H}}\right)\left(1-\frac{\tanh\left(7.4939(i-0.8610)\right)\frac{W^{1/3}\cos i}{H}}{1-0.015163\frac{W^{1/3}\cos i}{H}}\right) \quad (26)$$

where i is in rad, W in kg and H in m; the numerical coefficients are dimensional and are valid only for these units.

3.5 Validation of equation

As for experimental groups, the fitting residual reflection coefficients based on the new established Eq. (26) are calculated in Table 7. The calculated values of residual reflection coefficients are in good agreement with experimental results. So, it is verified that Eq. (26) is fit for subsequent design and engineering evaluation.

Table 7 Comparison of residual reflection coefficients

Test Serial Numbers	Corresponding position	Residual reflection coefficient		Error (%)
		Test values	Formula calculated value	
S-1	A1	0.364	0.364	0.0
	A2	0.425	0.455	7.1
	A3	0.4	0.461	15.2
S-2	A1	0.156	0.137	12.1
	A2	0.405	0.431	6.5
	A3	0.478	0.456	4.7
S-3	A2	0.349	0.336	3.6
	A3	0.43	0.448	4.1
S-4	A1	0.236	0.257	8.9

Test Serial Numbers	Corresponding position	Residual reflection coefficient		Error (%)
		Test values	Formula calculated value	
S-5	A2	0.651	0.557	14.4
	A3	0.439	0.453	3.2
	A1	0.118	0.129	9.6
	A2	0.506	0.423	16.6
	A3	0.393	0.448	13.9
S-6	A2	0.447	0.427	4.5
	A3	0.379	0.441	16.2

4 Threat assessment for underwater personnel

4.1 Impulse damage criteria

When conducting underwater blasting operations, operators are often required to work underwater. The explosive charge is detonated only after the operators have withdrawn to a safe area. However, the bottom interface can cause blast shock wave to reflect back, thus enhancing the strength of shock wave and extending the dangerous area for personnel. Previous studies show that the organs and tissues in the human body will be damaged when people are exposed to UNDEX shock wave [24]. Air-containing organs, such as lungs and gastrointestinal tract, are so sensitive that they are easily damaged. Due to the vulnerability, the lungs are often chosen as the typical organ to evaluate the degree of damage to personnel or creatures [25]. The impulse damage criteria proposed in reference [26] are adopted in this paper, and the damage grades and corresponding damage thresholds are shown in Table 8.

Table 8 Criteria for assessment of damage grades

Damage grade	Impulse (kPa·ms)	Symptoms
Mild injury	121.1-142.0	Petechial and patchy pulmonary hemorrhages, dilation of alveolar septa
Moderate injury	142.1-214.3	Localized pulmonary lacerations, gastrointestinal serosal and submucosal hemorrhages
Transition zone	214.4-247.8	Symptoms transitioning between moderate and severe injuries
Severe injury	247.9-322.6	Extensive pulmonary lacerations, laceration of mucosal layer of small intestine, subcapsular hematomas of the liver and spleen
Very severe injury	322.7-579.8	Severe pulmonary hemorrhagic edema, gastrointestinal perforations, hepatic and splenic ruptures
Beyond very severe injury	> 579.9	Extremely severe or fatal injuries, massive organ destruction

4.2 Calculation of the damage zones

To quantify the influence of the reflected wave on the UNDEX damage zones, two series of calculations are performed, with and without a reflecting bottom. The impulse is evaluated on a uniform 0.5 m grid over a domain 1200 m wide and 1000 m high, with the seabed at y = 0 and the charge at a stand-off distance H = 200 m. In the F series the bottom is removed and the impulse is taken as the closed-form $P_{m1}\theta$, i.e. Eq. (1) integrated over $0 \le t \le \theta$ only. This is the conventional estimate adopted in the literature and is retained deliberately, so that the two series differ only by the reflected arrival. In the R series the reflected arrival of Section 2.1 is superposed on the direct one, each arrival retaining the waveform of Eq. (1) truncated at 10θ so that its integral equals $1.4795P_{m1}\theta$; the reflection coefficient of Eq. (26) gives P_{m2} and θ_r. The simulation conditions are shown in Table 9.

Table 9 Calculation conditions for the damage zone

Group name	Charge mass (kg)	Presence of reflecting bottom (With/Without)
R-1	1	With
R-2	3	With
R-3	5	With
F-1	1	Without
F-2	3	Without
F-3	5	Without

Note: the charge is placed at a stand-off distance H = 200 m above the seabed. The reflected cases use the image-source model of section 2.1; the F cases omit the bottom entirely.

By using theoretical calculation model of reflection coefficient for UNDEX shock wave, the impulse is calculated by integrating the pressure with respect to time. The UNDEX damage zones are obtained on the basis of impulse damage criterion, as shown in Fig. 12.

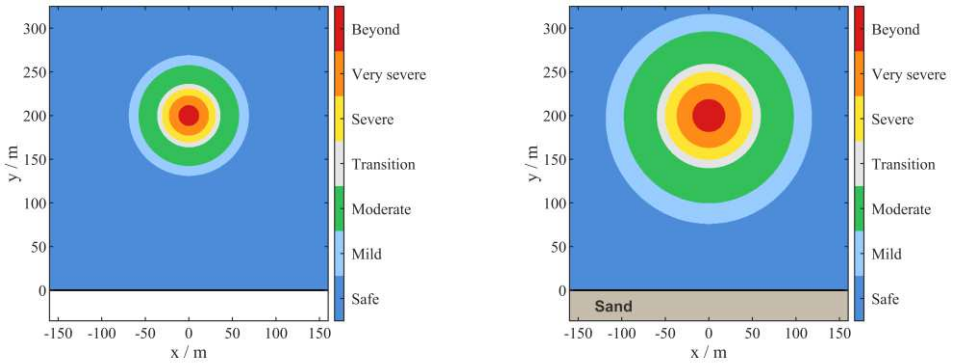

(a) F-1 damage-level contour map (b) R-1 damage-level contour map

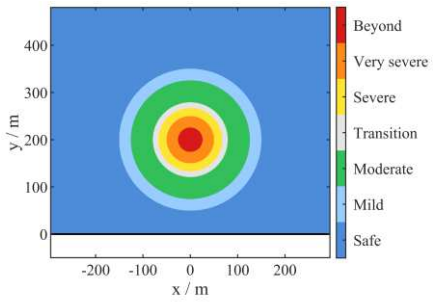

(c) F-2 damage-level contour map

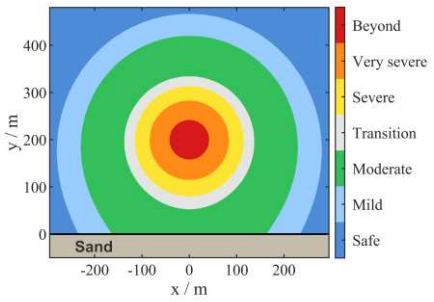

(d) R-2 damage-level contour map

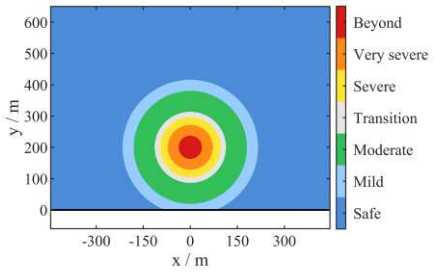

(e) F-3 damage-level contour map

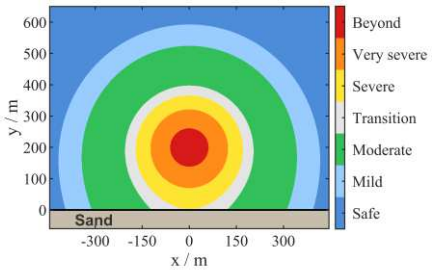

(f) R-3 damage-level contour map

Fig. 12 Calculation results of damage zone for different conditions (F: free field; R: with reflecting bottom). In the color bar, "Beyond" denotes the beyond very severe grade

In accordance with calculated damage zones, the maximum radii can be given for different damage grades, as exhibited in Table 10.

Table 10 Calculation results of maximum damage radius (m)

Damage grade	R-1	F-1	R-2	F-2	R-3	F-3
Mild injury	118.0	69.0	279.5	150.0	416.5	215.5
Moderate injury	97.5	57.5	229.0	125.5	342.5	180.0
Transition zone	59.5	36.0	137.0	79.0	204.5	113.5
Severe injury	50.0	30.5	115.0	67.0	170.5	96.5
Very severe injury	37.0	22.5	83.5	49.5	123.0	71.5
Beyond very severe injury	18.5	11.5	41.5	25.5	61.0	37.0

Note: R and F denote the cases with and without the reflecting bottom; each value is the maximum radius at which the lower impulse limit of the grade is reached.

All maximum radii are plotted in a comparison graph (Fig. 13). It can be seen that the seabed significantly increases the effective damage area due to its reflection. For the 5 kg charge the outer (mild-injury) contour lies at 215.5 m without the bottom and at 416.5 m with it, a factor of 1.93. Of this factor, 1.19 is due to the reflected arrival alone (256.0 m when the reflected wave is superposed but both arrivals keep the closed-form $P_{m1}\theta$); the remaining 1.62 arises because $P_{m1}\theta$ omits the reciprocal

decay tail of Eq. (1). At 250 m from the axis in the 5 kg case the closed-form estimate gives 106.2 kPa·ms, below the 121.1 kPa·ms lower limit of mild injury, whereas the superposition model gives 182.4 kPa·ms, in the moderate-injury range; at 75 m in the 1 kg case the values are 112.5 and 174.9 kPa·ms. A location that the conventional estimate places in the lowest category is thus placed in a higher one once the reflected arrival is retained. Because both the charge masses and the biological criteria lie outside the validated scope of the reflection correlation and human-response data, respectively, the numerical distances should not be interpreted as safety boundaries.

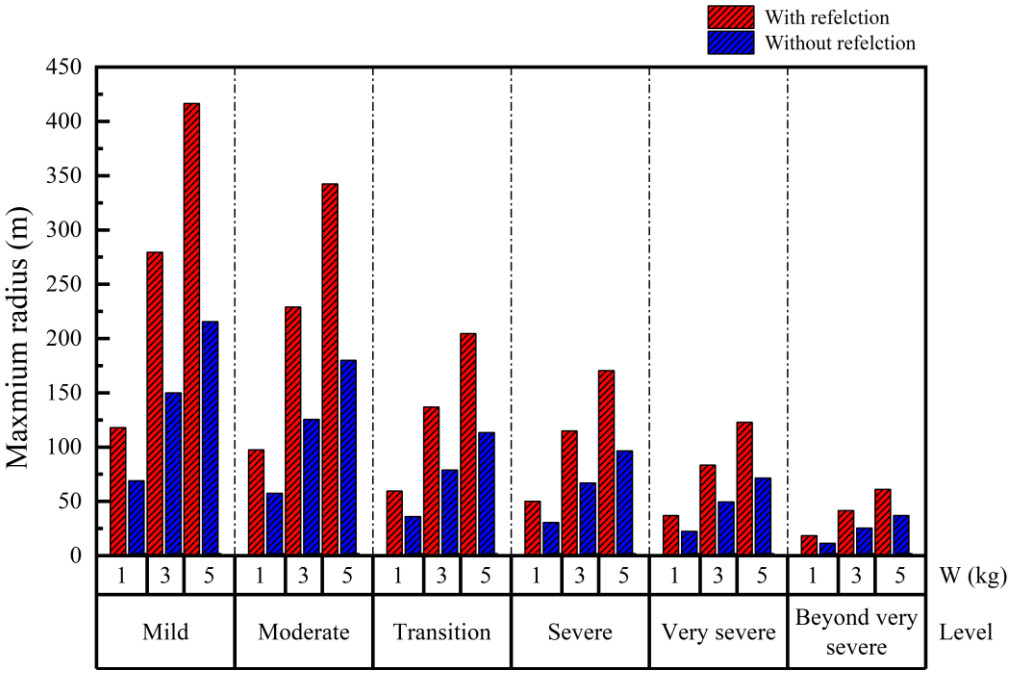

Fig. 13 Comparison of UNDEX damage zones with and without reflection surfaces

5 Conclusion

Through analytical derivation, tank experiments and ALE simulation, the reflection enhancement mechanism of the non-ideal sandy seabed to UNDEX shock wave is systematically revealed, and the impact of the reflection wave on the UNDEX damage zone was quantified. The main conclusions are summarized as follows:

(1) The theoretical model for solving the reflected wave pressure in sandy media proposed in this paper is accurate and efficient. The presented reflection coefficient model effectively corrects the overprediction bias arising from the traditional rigid wall assumption.

(2) The reflection of underwater shock waves on the surface of sand media is strongly angle-dependent. When the incident angle exceeds the critical angle of the longitudinal wave, the reflected longitudinal wave drops abruptly.

(3) The enhanced effect of sandy seabed causes a significant increase in the maximum underwater

damage radius, bringing areas on the seabed that were theoretically beyond safe distance to meet the damage criteria.

Although this study yields definitive conclusions, caution is needed when applying its findings to practical marine engineering due to inherent scale effects in physical modeling. Current model validation relies mainly on lab-scale explosion tests and idealized, homogeneous saturated sand seabed boundaries. Real-world seabeds, however, are geologically heterogeneous—featuring stratified sediments, spatially variable saturation, and diverse geotechnical properties.

CRediT authorship contribution statement

Jifeng Wei: Conceptualization, Methodology, Supervision, Writing – review and editing. **Xingwei Liu:** Investigation, Formal analysis, Writing – original draft. **Yuxuan Zheng:** Data curation, Visualization, Validation. **Fangfei Ren:** Software, Resources, Project administration. **Junjie Xiao:** Investigation, Validation. **Jialin Zhu:** Data curation, Formal analysis.

Declarations

Funding

This work was supported by the State Key Laboratory of Explosion

Science and Safety Protection (No. 202420241129A).

Competing interests

The authors declare that they have no competing interests.

Data availability.

The data that support the findings of this study are not publicly available due to security constraints of the research project. They are available from the corresponding author upon reasonable request.

References

1. Rajendran, R., Lee, J.M.: Blast loaded plates. Mar. Struct. 22(2), 99–127 (2009). https://doi.org/10.1016/j.marstruc.2008.04.001

2. Zhang, A.M., Yang, W.S., Yao, X.L.: Numerical simulation of underwater contact explosion. Appl. Ocean Res. 34, 10–20 (2012). https://doi.org/10.1016/j.apor.2011.07.009

3. Lance, R.M., Capehart, B., Kadro, O., Bass, C.R.: Human injury criteria for underwater blasts. PLOS ONE 10(11), e0143485 (2015). https://doi.org/10.1371/journal.pone.0143485

4. Schiffer, A., Tagarielli, V.L.: The response of rigid plates to blast in deep water: fluid–structure interaction experiments. Proc. R. Soc. A 468(2145), 2807–2828 (2012).

https://doi.org/10.1098/rspa.2012.0076

5. Cole, R.H.: Underwater Explosions. Princeton University Press, Princeton, NJ (1948). https://doi.org/10.5962/bhl.title.48411

6. Zamyshlyaev, B.V., Yakovlev, Y.S.: Dynamic Loads in Underwater Explosion. Report AD-757183, National Technical Information Service, Springfield, VA (1973).

7. Barras, G., Souli, M., Aquelet, N., Couty, N.: Numerical simulation of underwater explosions using an ALE method: the pulsating bubble phenomena. Ocean Eng. 41, 53–66 (2012). https://doi.org/10.1016/j.oceaneng.2011.12.015

8. Han, W., Dong, Y.F., Li, R.N., Zhang, Y.K., Bai, L.: Damage characteristics of ribbed cylinder in motion under near-field underwater explosion. AIP Adv. 14(2), 025218 (2024). https://doi.org/10.1063/5.0189360

9. Yu, W.L., Song, S., Choi, J.I.: Numerical simulations of underwater explosions using a compressible multi-fluid model. Phys. Fluids 35(10), 106102 (2023). https://doi.org/10.1063/5.0165384

10. Wang, Q.X.: Non-spherical bubble dynamics of underwater explosions in a compressible fluid. Phys. Fluids 25(7), 072104 (2013). https://doi.org/10.1063/1.4812659

11. Wang, G.H., Zhang, S.R., Yu, M., Li, H.B., Kong, Y.: Investigation of the shock wave propagation characteristics and cavitation effects of underwater explosion near boundaries. Appl. Ocean Res. 46, 40–50 (2014). https://doi.org/10.1016/j.apor.2014.02.003

12. Wang, P.G., Zhang, Z.J., Yan, Q.S., Zhang, C.: A substructure method for the transient response of vertical cylinders subjected to shock wave of underwater explosion. Ocean Eng. 218, 108128 (2020). https://doi.org/10.1016/j.oceaneng.2020.108128

13. Wu, Y.X., Shao, Y., Xie, Y.J., Gao, H.L., Zhang, Z.F.: Load characteristics of underwater explosion shock wave near seabed charge projectile. Chin. J. High Press. Phys. 38(1), 015102 (2024). https://doi.org/10.11858/gywlxb.20230744

14. Yan, F.H., Yue, S.L., Qiu, Y.Y., Wang, M.Y., He, Y.: Calculation of shock wave transmission and reflection pressures at water–soil interface. Explos. Shock Waves 44(11), 112201 (2024). https://doi.org/10.11883/bzycj-2023-0440

15. Li, S., Zhang, A.M., Han, R., Cui, P.: Experimental and numerical study of two underwater

explosion bubbles: coalescence, fragmentation and shock wave emission. Ocean Eng. 190, 106414 (2019). https://doi.org/10.1016/j.oceaneng.2019.106414

16. Bardiani, J., Kyaw Oo D'Amore, G., Sbarufatti, C., Manes, A.: Machine learning combined with numerical simulations: an effective way to reconstruct the detonation point of contact underwater explosions with seabed reflection. J. Mar. Sci. Eng. 13(3), 526 (2025). https://doi.org/10.3390/jmse13030526
17. Li, Z., Xing, L.S., Gao, C., Zhou, X.G.: Bayesian modeling and characterization of underwater explosion shock wave loads with parameter uncertainty. Explos. Shock Waves 46(8), 083401 (2026). https://doi.org/10.11883/bzycj-2025-0287
18. Gojani, A.B., Ohtani, K., Takayama, K., Hosseini, S.H.R.: Shock Hugoniot and equations of states of water, castor oil, and aqueous solutions of sodium chloride, sucrose and gelatin. Shock Waves 26(1), 63–68 (2016). https://doi.org/10.1007/s00193-009-0195-9
19. Jackson, D.R., Richardson, M.D.: High-Frequency Seafloor Acoustics. Springer, New York (2007). https://doi.org/10.1007/978-0-387-36945-7
20. Kugler, S., Bohlen, T., Forbriger, T., Bussat, S., Klein, G.: Scholte-wave tomography for shallow-water marine sediments. Geophys. J. Int. 168(2), 551–570 (2007). https://doi.org/10.1111/j.1365-246X.2006.03233.x
21. Jin, Z.Y., Xu, W.T., Yin, C.Y., Lei, Z.Y., Kong, X.S.: Correction method for initial conditions of underwater explosion. J. Mar. Sci. Eng. 13(4), 759 (2025). https://doi.org/10.3390/jmse13040759
22. Fan, R.Y., Lin, G.J., Zhang, H., Zhang, L.F., Sun, W.F.: Dynamic behavior of submerged cylindrical shells under combined underwater explosion, bubble pulsation, and hydrostatic pressure. Materials 18(4), 818 (2025). https://doi.org/10.3390/ma18040818
23. Esmaeili, M., Tavakoli, B.: Finite element method simulation of explosive compaction in saturated loose sandy soils. Soil Dyn. Earthq. Eng. 116, 446–459 (2019). https://doi.org/10.1016/j.soildyn.2018.09.048
24. Bar-Kochba, E., Iwaskiw, A.S., Dunn, J.M., Ott, K.A., Harrigan, T.P., Demetropoulos, C.K.: The dynamic response of human lungs due to underwater shock wave exposure. PLOS ONE 19(5), e0303325 (2024). https://doi.org/10.1371/journal.pone.0303325

25. Wang, L.F., Fang, Y.Q., Fu, J.Y., Dong, H.T., Ding, W., Dong, H.: A review on underwater explosion and its biological damage. 2025 IEEE 2nd International Conference on Energy and Electrical Engineering, pp. 1–11 (2025). https://doi.org/10.1109/EEE64897.2025.11162798

26. Yang, Z.H., Zhu, P.F., Jiang, J.X., Yin, Z.Y., Zhou, J.H., Li, X.Y., Ning, X., Liu, D.W., Feng, G., Zhang, L., Zhang, X.X., Yang, Z.L.: Bio-effects of underwater blast waves. Explos. Shock Waves 23(2), 134–139 (2003). https://doi.org/10.11883/1001-1455(2003)02-0134-6